Paper No.
13297

NACE INTERNATIONAL CORROSION Conference & Expo 2019

Corrosion of candidate materials for use in alkaline water electrolysis

M. Tjelta and Jon Kvarekvål
Institute for Energy Technology
P.O. Box 40, N-2027 Kjeller
Norway

ABSTRACT

In alkaline water electrolysis the capital expense (CAPEX) of the electrolyzer unit is high and cost reduction, wherever possible, is highly desired. Many parts are made of expensive nickel-based alloys, which in some cases may be an overly conservative option. Careful evaluation of the operating conditions may reveal that expensive alloys may be replaced by cheaper ones in parts of the system.

In this paper the corrosion behavior of candidate materials, relevant for use in atmospheric and pressurized alkaline water electrolysis systems, is evaluated at typical operating conditions (i.e. 1-30 bar pressure, 60-80 °C and 25 wt% KOH). The materials tested are one austenitic stainless steel (UNS S31603), one super duplex stainless steel (UNS S327X0) and one carbon steel (UNS K03014), with one nickel base alloy (UNS N06625) included in the matrix as a reference material.

Performance is evaluated based on mass loss corrosion and localized corrosion based on surface profilometry. Corrosion scales and their protectiveness are evaluated based on analysis using SEM/EDS and XRD. Carbon steel was found to have lower corrosion rates than the other steels at all temperatures.

Key words: Alkaline, water electrolysis, CRA, corrosion

INTRODUCTION

The global renewable energy market is fast growing with a focus on solar and wind. These are intermittent energy sources that are subject to both seasonal and hourly variations, generating significant amounts of excess energy (several TWh/year worldwide) that will have to be stored before utilization. Power-to-Gas technologies, such as water electrolysis, are expected to play a major role in future energy storage systems. Hydrogen production by water electrolysis is highly appropriate for storage of large amounts of intermittent renewable energy.

Although polymer electrolyte membrane (PEM) electrolyzers have the best performance for water electrolysis, the complexity of the system with its high pressure operation and the high cost – mainly due to the use of noble metal catalysts – have prevented commercialization thus far.[1,2]

An established alternative is alkaline water electrolysis. These operate at lower current densities, but are less expensive and thereby suitable for large-scale hydrogen production.[3] Current R&D typically aim to increase efficiency and decrease operational expenses (OPEX). Strategies to do this typically decreasing the cell voltage, which can potentially be achieved by zero-gap systems,[3] or increasing the current density and operating pressure.[2]

Electricity cost and other OPEX will vary with time and their contribution to the total life cycle cost is uncertain at the time of purchase. Reduced capital expenses (CAPEX) are therefore expected to make the use of alkaline electrolyzers more economically attractive. Materials for the various parts of the electrolyzer (cell stacks, separators, electrolyte loops etc.) are a significant part of the CAPEX, especially for pressurized electrolyzers. A strategy towards reducing the total cost of an electrolyzer system is therefore to cut down on the use of the most expensive alloys (nickel-based) and explore the possibility of using cheaper options such as stainless or carbon steels with or without coating/cladding.

In this work, four materials (UNS numbers N06625, S31603, S327X0 and K03014) are tested in 25 % KOH with 30 bar O_2 at temperatures ranging between 25 and 80 °C to evaluate corrosion and scale formation and potential applicability in alkaline water electrolyzers.

EXPERIMENTAL PROCEDURE

Corrosion tests

Corrosion tests were performed in 2 L UNS N10276 autoclaves, filled with 1.5 L of a solution made of 25 wt% KOH in distilled water. The solutions were purged with nitrogen before use to remove dissolved CO_2. In all tests, the partial pressure of oxygen was 30 bar. Magnetic stirring was enabled during the experiments.

Test specimens were disc-shaped coupons with a diameter of 2.5 cm and a thickness of 3 mm made of carbon steel (K03014), stainless steel (S31603), super duplex (S327X0) and a nickel base alloy (N06625). Coupons were suspended in the autoclave using PTFE or PEEK holders.

Experiment A01 was performed at 80 °C and had one specimen of each material in the same autoclave. In experiments A02-1 and A02-2, the temperature was 25 °C and the first one had two carbon steel specimens while the other had two specimens of both S31603 and S327X0. No N06625 was exposed in these experiments. The distribution of coupons in A03-1 and A03-2, which were carried out at 60 °C, were the same. A summary of the experimental conditions and test materials is shown in Table 1, and alloy compositions are given in Table 2 and Table 3. Mass loss corrosion was evaluated after removing the corrosion film with Clark's solution.

X-ray diffraction

X-ray diffraction of the corrosion coupons were performed as-is, meaning that the full assembly of substrate, corrosion film and deposits were placed in a custom-made holder in the diffractometer. For some samples, diffractograms were recorded both with loose deposits intact and with them wiped off.

SEM/EDS analysis

The top-side of the corrosion coupons were investigated in SEM and EDS analysis were performed. No chemical treatment was performed prior to analysis, but any loose deposits were removed using pressurized air.

3D-Profilometry

After investigation on SEM/XRD the corrosion coupons were stripped of their corrosion films using inhibited hydrochloric acid. The coupons were then scanned with a 3D profilometer using white light

axial chromatism. The scan grid size was 10 µm x 10 µm with a vertical resolution of about 75 nm. An optical pen with 300 µm pen vertical range was used unless stated otherwise.

Table 1: Summary of experimental conditions

Exp. ID	Test material UNS	Temp. [°C]	Electrolyte composition	O_2 pressure [bar]	Specimen A [cm^2]	Duration [days]
A01	K03014	80	25 wt% KOH	30	12.17	35
A01	S31603	80	25 wt% KOH	30	12.17	35
A01	S327X0	80	25 wt% KOH	30	12.17	35
A01	N06625	80	25 wt% KOH	30	12.17	35
A02-1	K03014	25	25 wt% KOH	30	12.17	35
A02-2	S31603	25	25 wt% KOH	30	12.17	35
A02-2	S327X0	25	25 wt% KOH	30	12.17	35
A03-1	K03014	60	25 wt% KOH	30	12.17	28
A03-2	S31603	60	25 wt% KOH	30	12.17	28
A03-2	S327X0	60	25 wt% KOH	30	12.17	28

Table 2: Alloy composition 1

UNS	Fe		Cr		Ni		Mo		Co		Cu		Nb + Ta	
	Min	Max	Min	Max	Min	Max	Min	Max	Min	Max	Min	Max	Min	Max
K03014	Bal.		-	-	-	-	-	-	-	-	-	-	-	0.05
S31603	Bal.		16	18	10	14	2	3	-	-	-	-	-	-
S32750	Bal.		24	26	6	8	3	5	-	-		0.5	-	-
S32760	Bal.		24	26	6	8	3	4	-	-	0.5	1	-	-
N06625	-	5	20	23	58	-	8	10	-	1	-	-	3.15	4.15

Table 3: Alloy composition 2

UNS	W		Mn	C	P	S	N		Al	Si	Ti	V
	Min	Max	Max	Max	Max	Max	Min	Max	Max	Max	Max	Max
K03014	-	-	1.65	0.16	0.02	0.01	-	-	-	0.01	0.06	0.09
S31603	-	-	2	0.03	0.045	0.03	-	0.1	-	0.75	-	-
S32750	-	-	1.2	0.03	0.035	0.02	0.24	0.32	-	0.8	-	-
S32760	0.5	1	1	0.03	0.03	0.01	0.2	0.3	-	1	-	-
N06625	-	-	0.5	0.1	0.015	0.015	-	-	0.4	0.5	0.4	-

RESULTS

The exposed coupons were analyzed visually, and documented with pictures, before and after removal of corrosion films. Mass loss was used to obtain corrosion average corrosion rates and 3D profilometry was performed to look for localized attacks. In order to elucidate possible corrosion film products, both XRD and SEM/EDS were carried out.

Corrosion rates

Mass loss corrosion rates are summarized in table form in Table 4 and plotted as a function of temperature in Figure 1.

It should be mentioned that the reported mass loss corrosion rates for carbon steel, at least at 25 and 60 °C, are probably overconservative, since the acid treatment used to remove the film also resulted in additional corrosion after the film was gone. For S31603 and S327X0, however, corrosion rates are probably underestimated since complete removal of the films proved very difficult.

The fact that the inner films at UNS S31603 and S327X0 could not be completely removed after treatment in inhibited HCl showed that they adhered very well to the substrate and probably also offered protection against further corrosion. A well-known shortcoming of using mass loss corrosion rates only is that the reported value is averaged over the entire duration of the experiment, hence the development with time is not obtained. This means that a high corrosion rate in the initial stage of the experiment will contribute significantly to the average mass loss corrosion rate, although the corrosion rate at the end of the experiment may be negligible due to the formation of a protective film.

UNS S327X0 showed a larger corrosion rate than S31603 did at the higher temperatures. Interestingly, the carbon steel showed lower corrosion rates than S31603 and S327X0 at all temperatures. This contrasts experience from corrosion science related to oil and gas. Here it is generally considered that S327X0 performs better than S31603 in oxidizing environments, and that both of them are generally more corrosion resistant than carbon steel. The pH in the two applications is, of course, vastly different.

The Caustic Soda Service Chart in NACE International standard RP0403 [4] suggests that carbon steel can be used the temperature and KOH level investigated in this work, as long as it proper stress relief is applied.

Table 4: Mass loss corrosion rates in µm·year^{-1}

Test material	Temperature / °C		
	25	60	80
K03014	0.5	7.5	16.4
S31603	2.7	11.4	41.3
S327X0	0.5	41.5	63.4
N06625	-	-	0.7

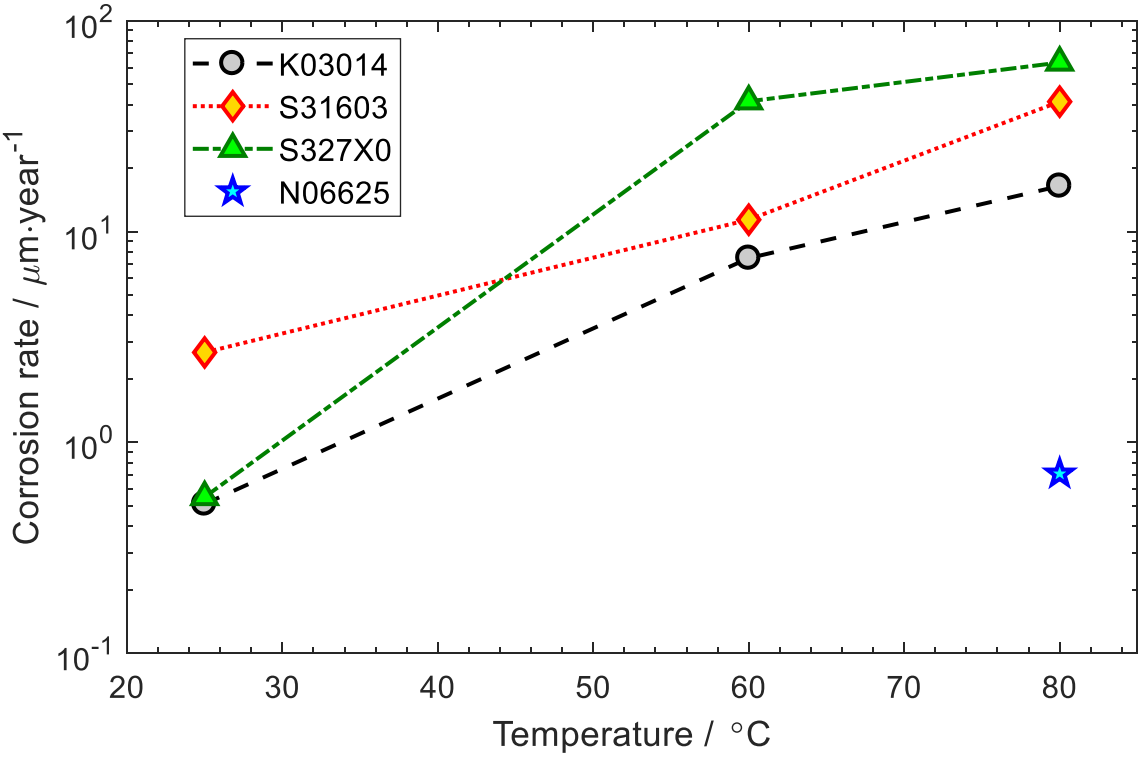

Figure 1: Mass loss corrosion rates for the different alloys as a function of temperature

Visual observation and surface profiles

Figure 2 a, b and c show pictures of carbon steel corrosion coupons, with all corrosion products still intact, from the experiments at 25, 60 and 80 °C. In Figure 3, pictures of the same coupons are shown after treatment in inhibited HCl and Figure 4 shows false color surface profiles of the stripped surfaces. The color representation in a paper may, for various technical reasons, not represent the actual color of the specimen. Therefore, the observe color of the various corrosion coupons are summarized in Table 5 to be used as a guide to the pictures in Figure 2, Figure 5 and Figure 8.

Figure 5 shows pictures of S31603 corrosion coupons with films, Figure 6 shows the same pictures after HCl treatment and Figure 7 show the surface profiles. In all the figures, a, b and c are from the 25, 60 and 80 °C experiments, respectively.

Figure 8, Figure 9 and Figure 10 show pictures of S327X0 corrosion coupons, pictures of stripped coupons and surface profiles of stripped coupons with the temperature increasing from left to right across the figures.

N06625 was only exposed at 80 °C as a reference experiment. Both corrosion and corrosion products were essentially absent, meaning that this material apparently passed the test in the most severe conditions and was not studied further. It should, however, be mentioned that leaching or dealloying of Mo from N06625 is possible.[5]

Corrosion films formed were visually absent for carbon steel exposed at 25 °C and N06625, which can be seen in pictures of the corrosion coupons after exposure, cf. Figure 2 a and Figure 11 a, respectively (N06625 was only exposed at 80 °C). Here the corrosion coupons look essentially unaffected by the exposure. This means that thin protective films were formed.

Carbon steel exposed at 60 °C (Figure 2 b.), S31603 exposed at 25 and 60 °C (Figure 5 a and b) and S327X0 exposed at 25 °C (Figure 8 a) had thin corrosion films with colors typical of thin-film interference. The apparent stripes typically follow the striped tool-marks from machining.

At 80 °C, both carbon steel, S31603 and S327X0 formed fairly thick corrosion films, with S327X0 having the thicker one. S327X0 also formed a fairly thick film at 60 °C where the other substrates only formed interference-type films.

Table 5: Color of corrosion products (to be used as an aid to Figure 2, Figure 5 and Figure 8)

Test material	Layer	Temperature [°C]		
		25	60	80
UNS K03014	Upper Lower	Steel	Blue, rainbow	Brown/rusty Dark blue
UNS S31603	Upper Lower	Golden rainbow	Burgundy/rainbow	Black/grey
UNS S327X0	Upper Lower	Rainbow	Red Brown/blue/black	Blue/green/grey Brown/red
UNS N06625	-	-	-	Steel

A relationship between the color of thin thermally grown SiO_2 and thickness was established in the 60's.[6] By scaling those values with the refractive index, an estimate of the color of other films can be obtained, e.g. as given for magnetite anodically grown on a steel substrate.[7] A careful assignment of film thickness based on color will not be attempted here, but we suffice to say that the interference-colored films are some 100 nm while the opaquer ones are in the µm range. Such film thickness is also obtained from the mass loss, as shown in Table 6, where film density has been assumed based on typical surface oxide for the given substrate.

Table 6: Film thickness in µm obtained from mass loss using assumed film density

Test material	Temperature [°C]			Assumed density $g \cdot cm^{-3}$
	25	60 *	80	
UNS K03014	0.1	0.4	2.5	5.3 (Fe_2O_3 or Fe_3O_4)
UNS S31603	0.3	0.6	2.6	5.37 ($NiFe_2O_4$)
UNS S327X0	0.1	2.0	7.1	5.37 ($NiFe_2O_4$)
UNS N06625	-	-	0.2	5.37 ($NiFe_2O_4$)

* the 60 °C experiment had a duration of 28 days (cf. 35 days for 25 and 80 °C)

Surface profiles of the corrosion coupons after film removal did not show any particular localized attack, except from some pit-like attacks in the S327X0 coupon exposed at 80 °C (cf. Figure 10 c). The general feature of the other coupons is that of the stripes from machining, apart from carbon steel exposed at 80°C which showed a roughened surface (cf. Figure 4 c).

UNS K03014

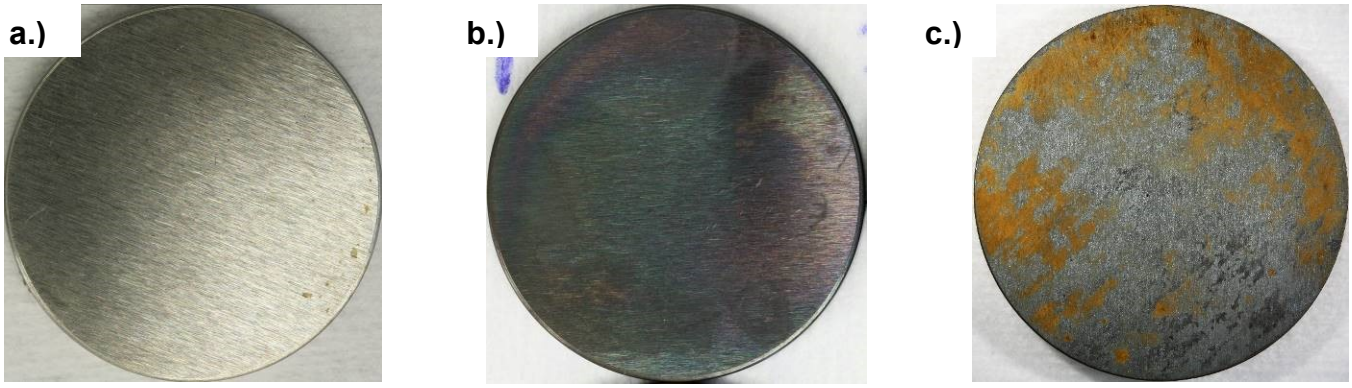

Figure 2: Pictures of carbon steel coupons after exposure at (a) 25 °C, (b) 60 °C and (c) 80°C with the corrosion films intact

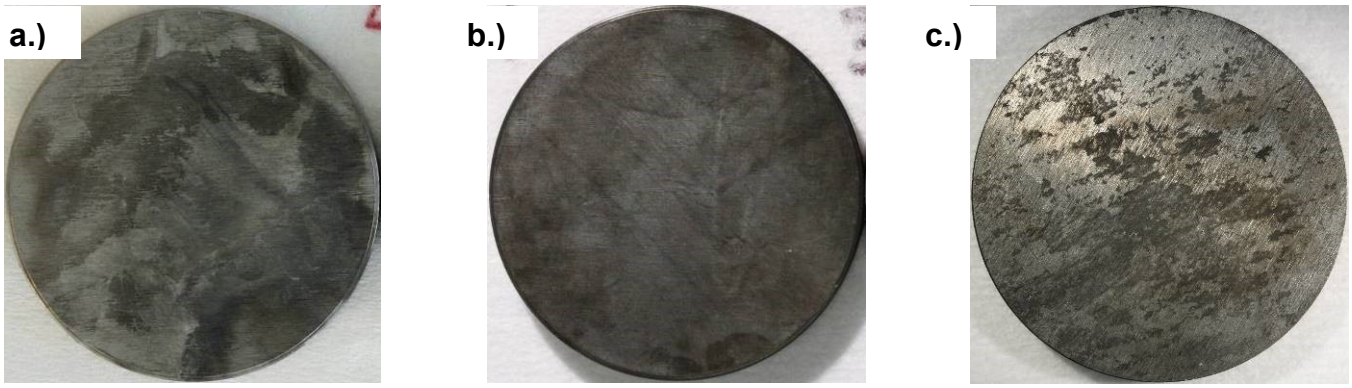

Figure 3: Pictures of carbon steel coupons after exposure at (a) 25 °C, (b) 60 °C and (c) 80°C after stripping in HCl

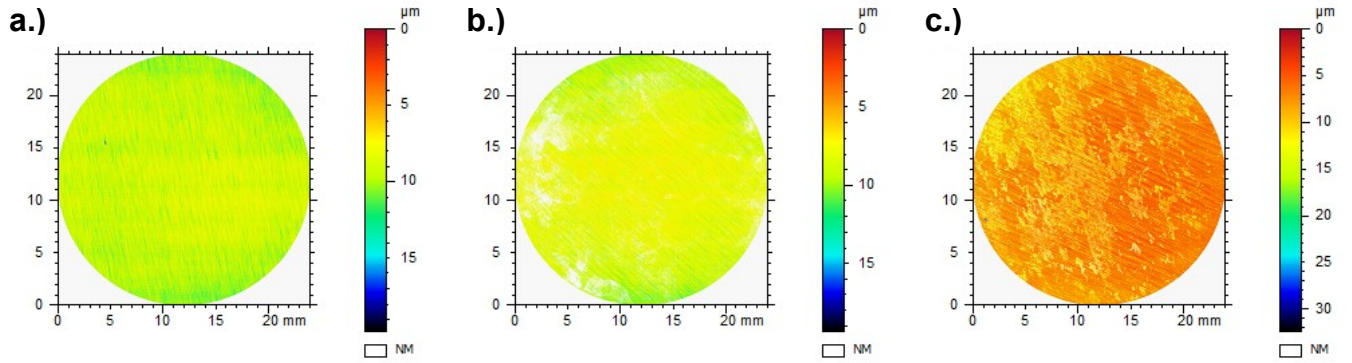

Figure 4: Surface profiles of carbon steel coupons after exposure at (a) 25 °C, (b) 60 °C and (c) 80°C with the corrosion films removed

UNS S31603

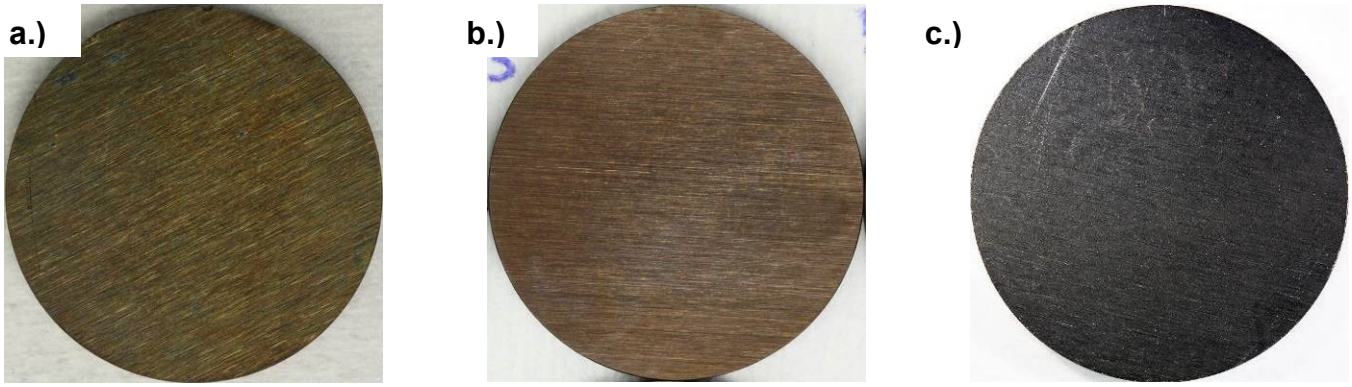

Figure 5: Pictures of S31603 coupons after exposure at (a) 25 °C, (b) 60 °C and (c) 80°C with the corrosion films intact

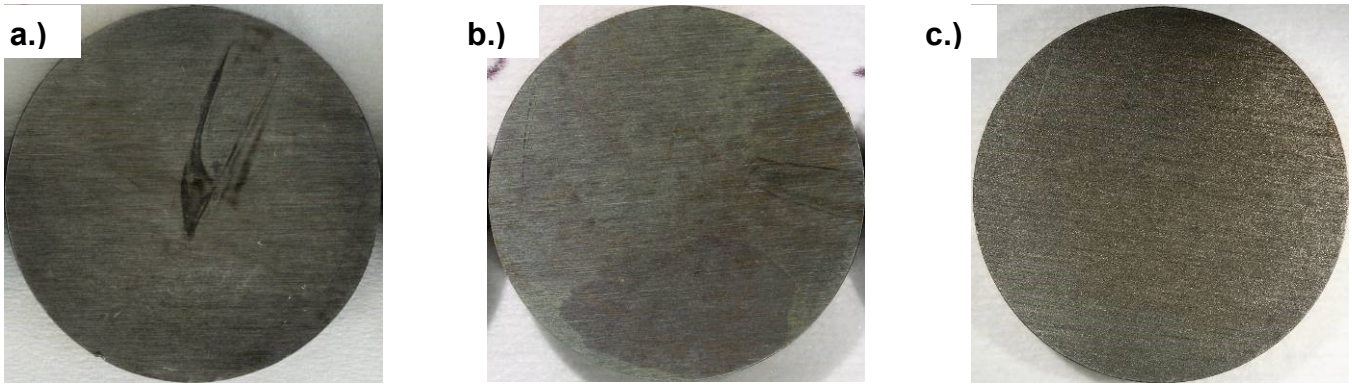

Figure 6: Pictures of S31603 coupons after exposure at (a) 25 °C, (b) 60 °C and (c) 80°C, after stripping in HCl

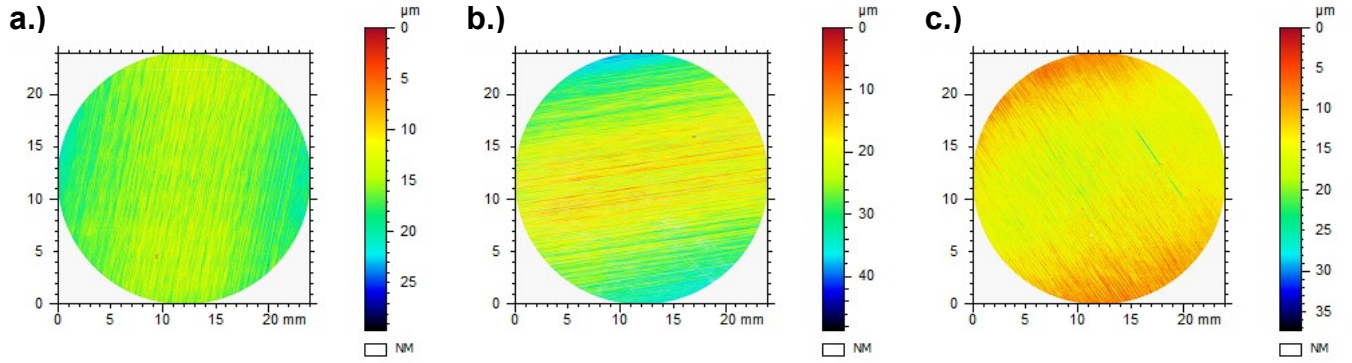

Figure 7: Surface profiles of S31603 coupons after exposure at (a) 25 °C, (b) 60 °C and (c) 80°C, after stripping in HCl

UNS S327X0

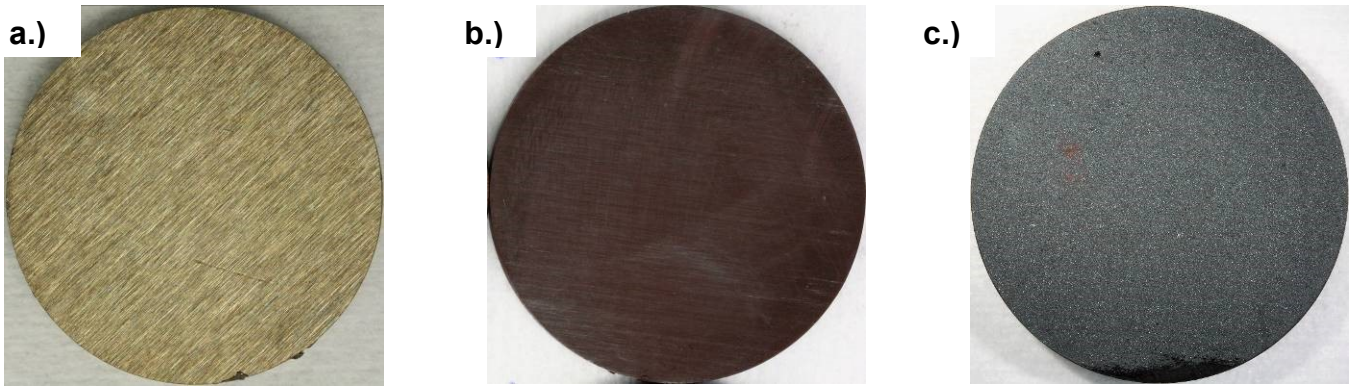

Figure 8: Pictures of S327X0 coupons after exposure at (a) 25 °C, (b) 60 °C and (c) 80°C with the corrosion films intact

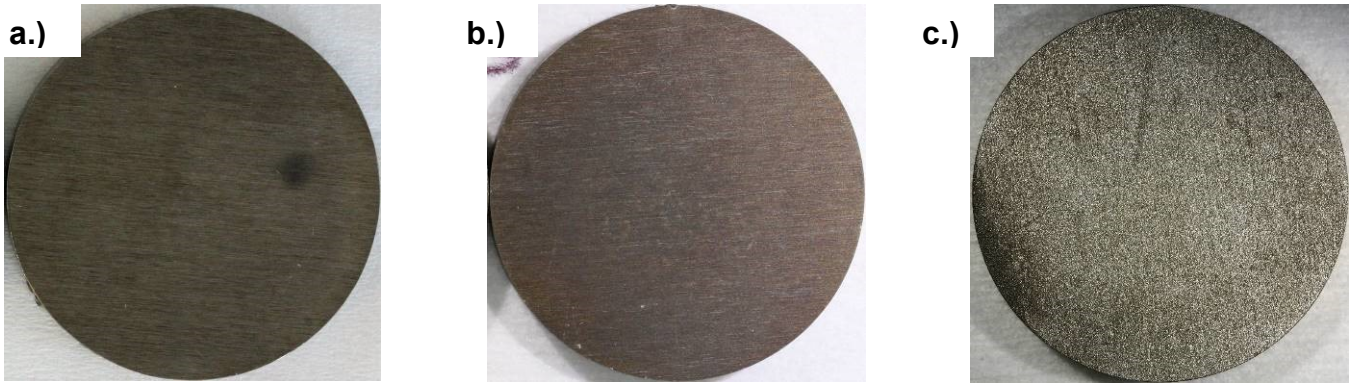

Figure 9: Pictures of S327X0 coupons after exposure at (a) 25 °C, (b) 60 °C and (c) 80°C, after stripping in HCl

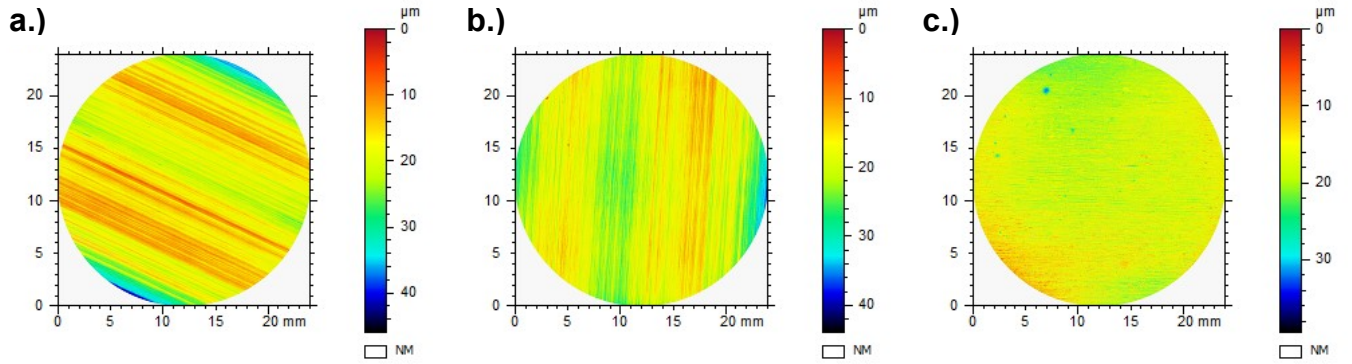

Figure 10: Surface profiles of S327X0 coupons after exposure at (a) 25 °C, (b) 60 °C and (c) 80°C, after stripping in HCl

UNS N06625

a.) b.)

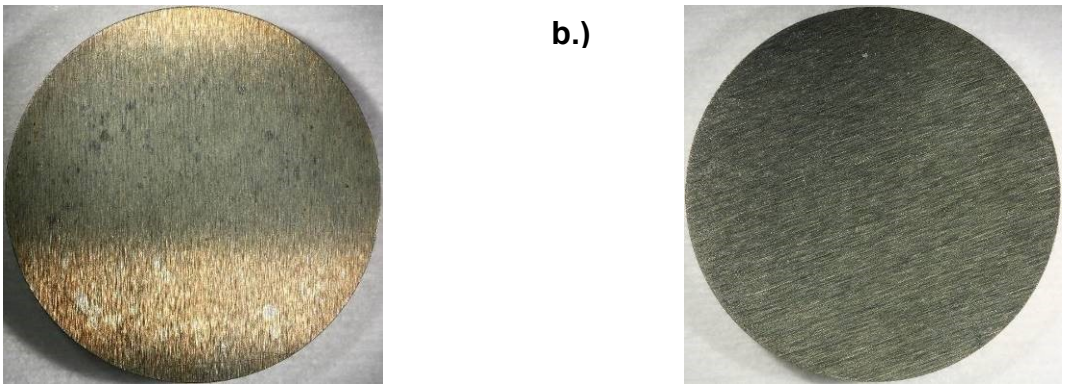

Figure 11: Pictures of an N06625 coupon after exposure at 80 °C, a.) with the corrosion film intact and b.) with the corrosion film removed. Note that the darker horizontal band of a.) is a shadow and not discoloration.

SEM

A selection of top-side SEM images is shown in this section. They will only be introduced here and rather discussed further together with the XRD results below. EDS spectra will not be explicitly shown, except from one example (super duplex at 25 °C), but the main elements detected will also be mentioned at the XRD results are discussed.

From EDS, small amounts of K were found to be present on most of the corrosion coupons. This does not mean that it was part of a corrosion product and it may very well have precipitated as a salt during the shut-down procedure of the experiment.

Images from the 25 °C experiments are not shown. From the 60 °C experiments, the S327X0 corrosion coupon is shown in Figure 12. Figure 13 shows carbon steel and S31603 and Figure 14 shows S327X0 and N06625 corrosion coupons from the 80 °C experiment.

a.) b.)

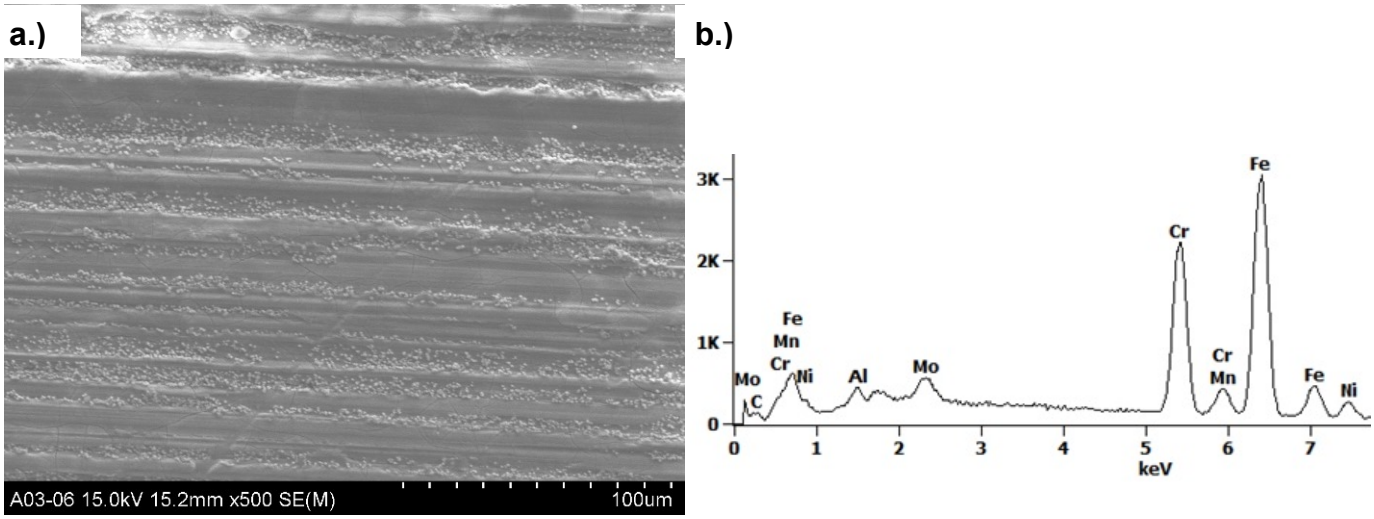

Figure 12: a.) SEM image S327X0 exposed at 60 °C and b.) EDS spectrum of the S327X0 film formed at 25 °C

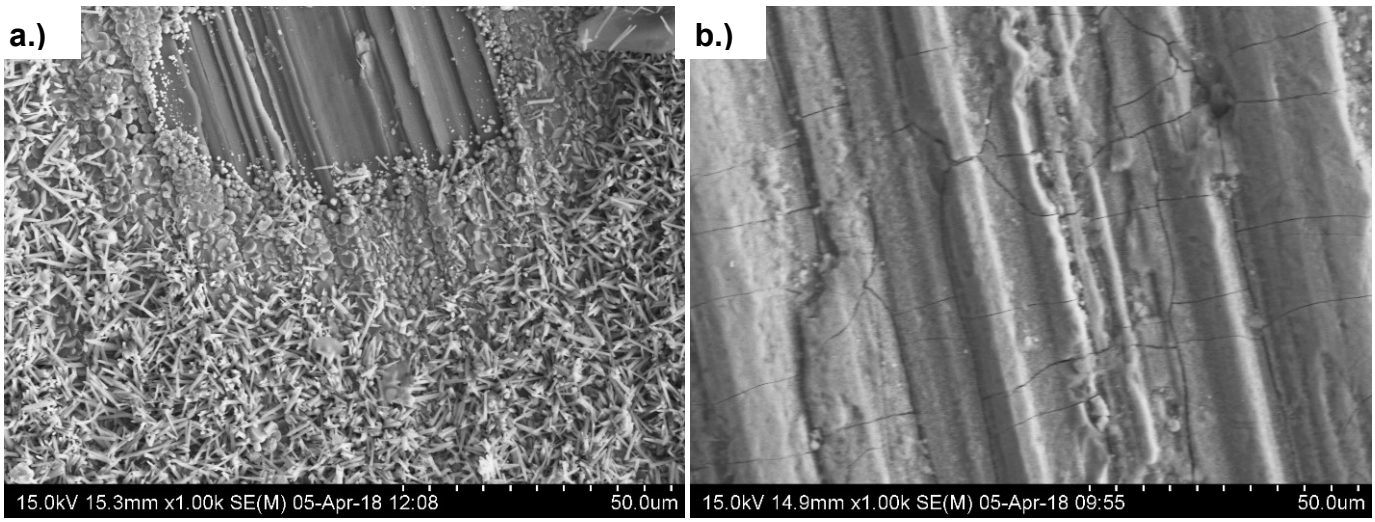

Figure 13: SEM images of a.) carbon steel and b.) S31603 exposed at 80 °C

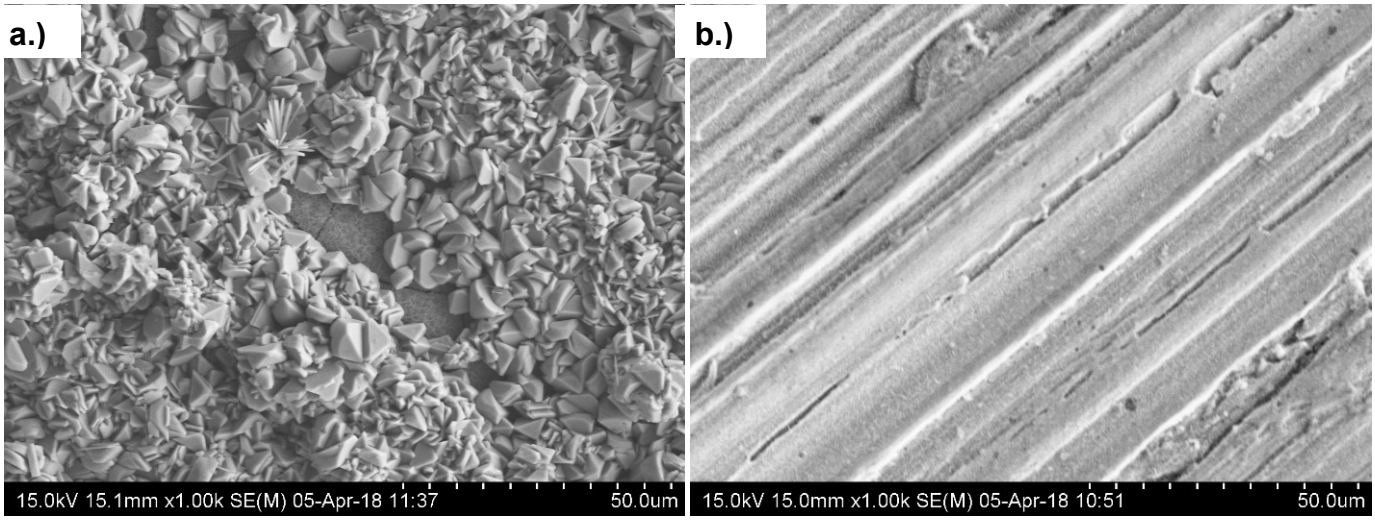

Figure 14: SEM images of a.) S327X0 and b.) N06625 exposed at 80 °C

X-ray diffraction

Interpretation of results from conventional Bragg-Brentano X-ray diffraction on the thin-films were complicated by the inherent geometry of the technique. The diffractograms showed mainly reflections from the different substrates, but by using long counting times it was possible to resolve some reflections attributed to the films. Grazing incidence XRD was also attempted, but since the roughness of the un-exposed coupons were larger than the film thickness, typical low gracing angles could not be used without giving a significant signal contribution from the substrate. Figure 15 shows a cartoon-like illustration of the difference between an ideal atomically flat surface and a rough surface. X-ray diffractograms for carbon steel, S31603 and S327X0 corrosion coupons are shown in Figure 16 through Figure 18.

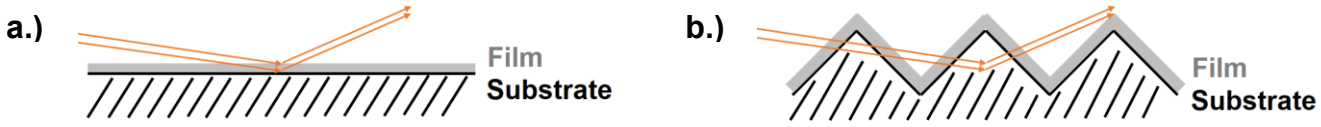

Figure 15: Illustration of a.) the ideal situation for gracing incidence XRD, and b.) the situation at a rough surface

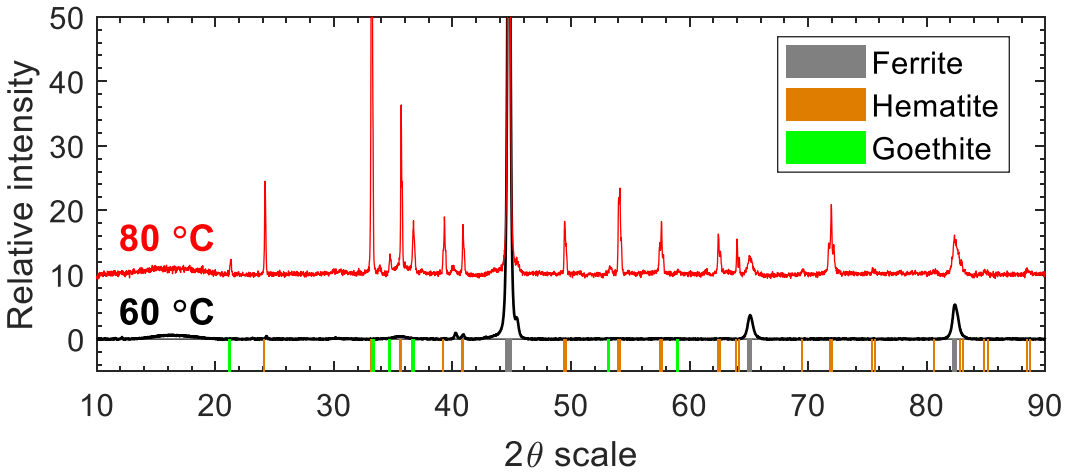

Figure 16: X-ray diffractograms of carbon steel corrosion coupons exposed at different temperatures

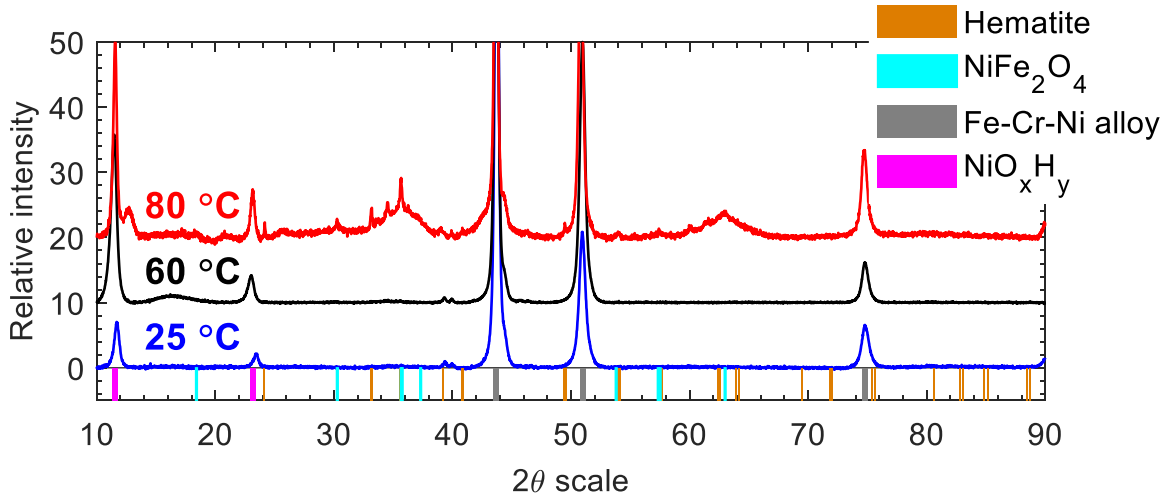

Figure 17: X-ray diffractograms of S31603 corrosion coupons exposed at different temperatures

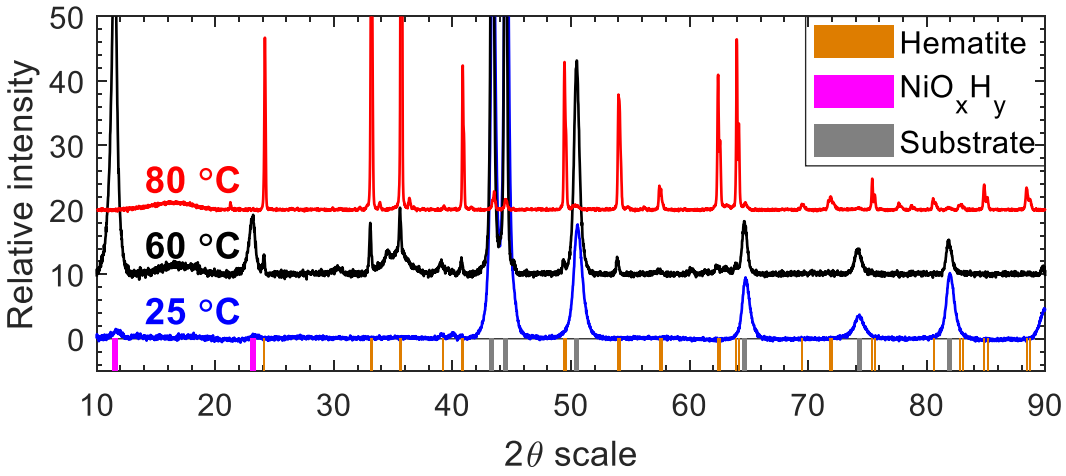

Figure 18: X-ray diffractograms of super S327X0 coupons exposed at different temperatures

UNS K03014

Due to the absence of a visible corrosion film, XRD was not carried out for carbon steel exposed at 25 °C. SEM showed a few deposits on the surface, which are believed to be hematite. EDS indicated Fe with some Mn, but no oxygen could be detected at the surface.

For carbon steel exposed at 60 °C, it was possible to resolve some minor XRD reflections, cf. Figure 16, with intensity below 1 % of the main reflection from the substrate (based on maximum counts, not integrals). Two of the reflections correspond to a spinel phase. Magnetite is the most likely candidate here, since only carbon steel coupons was exposed in the autoclave. However, if some nickel were present – either from dissolution of the autoclave or as a contaminant from a previous experiment – $NiFe_2O_4$ could also be present in the corrosion film. Some nickel in the surface film is suggested by EDS. Weak additional reflections have not been assigned to any phase, but we note that EDS suggested the presence of K and Mn.

Corrosion products at carbon steel exposed at 80 °C were mainly hematite and possibly small amounts of goethite according to XRD, cf. Figure 16. This fit very well with crystal habits seen in the SEM images, where plates and rhombohedra are typical for hematite and needles are typical for goethite.[8]

UNS S31603

X-ray diffractograms of S31603 exposed at 25 and 60 °C were qualitatively similar as seen in Figure 17. The substrate dominated the response, and they both had four reflections from secondary phases. Two minor reflections around 30° 2θ could originate from NiO and the two reflections at lower angles are most likely from a phase in the $Ni(OH)_2$-NiO(OH) system. The latter is a complex system with the possibility of cation substitution, anion incorporation between layers, hydration and stacking faults.[9] Thus, there are several possibilities and a definite conclusion on exactly which phase is present have not been made. EDS suggested a Fe-Ni-Cr oxide with minor amounts of Mn and possibly Mo.

The coupon exposed at 80 °C had some minor reflections, in addition to those from nickel oxide or oxy-hydroxide, some of which were assigned to hematite and $NiFe_2O_4$. Elements detected by EDS were Fe and Ni with some Cr and Mn in addition to minor amounts of K. SEM images showed that the film had cracks, but these may have formed during the drying process.

UNS S327X0

X-ray diffractograms for S327X0 are shown in Figure 18. At the coupon exposed at 25 °C some minor reflections from $Ni(OH)_2$/NiO(OH) was found, suggesting a thinner layer than in the case of S31603. The same conclusion was drawn based on mass loss (cf. estimated film thickness in Table 6). EDS did not detect oxygen and the main elements found were Fe, Ni and Cr. The EDS spectrum from an area of the film is shown in Figure 12 b.

Apart from the substrate, the major phase detected by XRD at the 60 °C was $Ni(OH)_2$/NiO(OH). The relative intensity of the reflections was larger than at the 25 °C coupon, suggesting a thicker, in line with the values in Table 6. Analysis of EDS data suggested the presence of Fe, Ni and Cr and here also O was detected. SEM images revealed a cracked layer, but again, such cracks may form during the drying process.

SEM images of the film formed at 80 °C showed an outer layer of rhombohedral particles. EDS suggested Fe end O. Combined with the fact that hematite was detected by XRD, we conclude that the outer layer was Fe_2O_3. Some needle-shaped islands were seen in the images, which is believed to be goethite based on crystal habit. The main constituents in the inner layer were Fe, Ni and O according to

EDS. It is possible that the nickel oxide/hydroxide was present in an inner layer of the corrosion film, but that the relatively thick hematite layer on top made it inaccessible to detection by XRD.

UNS N06625

N06625 was only exposed at 80 °C. XRD (not shown) indicated the presence of a $Ni(OH)_2$/NiO(OH) layer. Here EDS detected oxygen, although visual inspection (Figure 11) and mass loss (Table 6) suggested a very thin layer.

Corrosion scales and protection

Both at S31603, S327X0 and at N06625, the same low-angle reflections were present, indicative of a nickel oxide/hydroxide. According to Pourbaix diagrams calculated using OLI Studio,[10] the spinel $NiFe_2O_4$ is thermodynamically stable phase at alloys containing both nickel and iron when exposed to alkaline oxidizing conditions. At a pure nickel surface, the software gives the nickel spinel Ni_3O_4 as the stable phase. Experimentally, however, nickel hydroxides are often found as corrosion products on nickel metals and alloys.[11] These are, however, considered not to offer corrosion protection,[12] but merely act as a diffusion barrier. Below the hydroxide layer, an inter thin film of NiO or $NiFe_2O_4$ is generally believed to be responsible for corrosion protection. Above 120 °C it have been found that the presence of an iron spinel greatly decreased the corrosion rate.[13]

Since all alloys produced corrosion films, the difference in average corrosion rate must be due to a difference in how well the layers protect the substrate against further corrosion. At temperatures relevant for alkaline electrolysis the main transport through a film (or scale) is along cracks and pores or along grain boundaries. In the absence of cross-sectional images, it is difficult to evaluate possible transport paths through the scales. Proper evaluation of cracks and pores from cross-sectional SEM would probably require the use of FIB (focused ion beam), since the cutting and grinding procedure required otherwise would mechanically damage the surface and obscure such small features.

Cations are transported out from the metal surface, typically along grain boundaries, while oxygen in transported inwards from the film-solution interface. The oxide tends to form inside the existing scale resulting in compressive stresses.[14] A large grain boundary density implies several transport paths and therefore less protection against corrosion. When it comes to forming the scale/film in the first place, however, a large grain boundary density at the alloy side is preferred since this can aid in enrichment of the alloy element(s) required to form the protective scale. Hence, microstructure and heat treatment are important factors in such a picture.

Another possible effect is the difference in diffusion coefficients for different cations. For example, if nickel, the base material in N06625, diffuses through its film at a slower rate than iron, the base material in S31603, does through its corresponding film, N06625 will in effect be more corrosion resistant.

Materials for use in alkaline electrolysis

S31603 and S327X0 developed significant corrosion layers at 80 °C. Even if they would develop to offer protection against further corrosion over time, the amount of corrosion products could be problematic as a contaminant for electrodes and membranes. S327X0 formed a relatively large amount of corrosion products also at 60 °C, while S31603 performed slightly better.

Carbon steel outperformed the two other steels at all temperatures. At 80 °C the amount of hematite formed may be an issue for electrodes and membranes. At 60 °C, however, the amount of corrosion products formed at carbon steel was very small. Hence, carbon steel appears as a candidate for further

studies for possible extended use in alkaline electrolyzers. Especially the possibility of caustic cracking should be investigated further.

CONCLUSIONS

Corrosion tests of carbon steel, S31603, S327X0 and N06625 have been performed in 30 bar O_2 and 25 wt% KOH up to 80 °C. N06625, included as a reference material, showed negligible corrosion.

Carbon steel performed better than S31603 and S327X0 at all temperatures tested and showed low corrosion rates and thin corrosion films up to 60 °C. Hence, carbon steel is interesting as a possible material to replace expensive nickel alloys, especially in lower temperature systems. The possibility of caustic cracking needs to be investigated further.

ACKNOWLEDGEMENTS

This work was performed within MoZEES, a Norwegian Centre for Environment-friendly Energy Research (FME), co-sponsored by the Research Council of Norway (project number 257653) and 40 partners from research, industry and public sector. Institute for Energy Technology is also acknowledged for funding the project.

REFERENCES

1. M. Carmo, D.L. Fritz, W. Maier, D. Stolten, (Invited) Alkaline Water Electrolysis Vs. PEM Water Electrolysis - Exploring Their Full Performance, Meeting Abstracts, MA2015-01 (2015) 1489.
2. O. Schmidt, A. Gambhir, I. Staffell, A. Hawkes, J. Nelson, S. Few, Future cost and performance of water electrolysis: An expert elicitation study, International Journal of Hydrogen Energy, 42 (2017) 30470-30492.
3. A. Manabe, M. Kashiwase, T. Hashimoto, T. Hayashida, A. Kato, K. Hirao, I. Shimomura, I. Nagashima, Basic study of alkaline water electrolysis, Electrochimica Acta, 100 (2013) 249-256.
4. Avoiding Caustic Stress Corrosion Cracking of Refinery Equipment and Piping, in: Standard RP0403, NACE International, Houston, 2003.
5. R.B. Rebak, Industrial Experience on the Caustic Cracking of Stainless Steels and Nickel Alloys - a Review, CORROSION/2006, (2006), paper no. 06501, NACE International, Houston
6. W.A. Pliskin, E.E. Conrad, Nondestructive Determination of Thickness and Refractive Index of Transparent Films, IBM Journal of Research and Development, 8 (1964) 43-51.
7. T.D. Burleigh, T.C. Dotson, K.T. Dotson, S.J. Gabay, T.B. Sloan, S.G. Ferrell, Anodizing Steel in KOH and NaOH Solutions, Journal of The Electrochemical Society, 154 (2007) C579-C586.
8. R.M. Cornell, U. Schwertmann, Crystal Morphology and Size, in: The Iron Oxides, 2004, pp. 59-94.
9. D.S. Hall, D.J. Lockwood, C. Bock, B.R. MacDougall, Nickel hydroxides and related materials: a review of their structures, synthesis and properties, Proceedings. Mathematical, Physical, and Engineering Sciences / The Royal Society, 471 (2015) 20140792.
10. OLI Studio, v. 9.3, OLI Systems Inc., (2016).
11. M. Yasuda, K. Fukumoto, Y. Ogata, F. Hine, Corrosion Behavior of Ni and Ni-Based Alloys in Concentrated NaOH Solutions at High Temperatures, Journal of The Electrochemical Society, 135 (1988) 2982-2987.
12. S.L. Medway, C.A. Lucas, A. Kowal, R.J. Nichols, D. Johnson, In situ studies of the oxidation of nickel electrodes in alkaline solution, Journal of Electroanalytical Chemistry, 587 (2006) 172-181.
13. J.M. Gras, P. Spiteri, Corrosion of stainless steels and nickel-based alloys for alkaline water electrolysis, International Journal of Hydrogen Energy, 18 (1993) 561-566.
14. D.J. Young, High Temperature Oxidation and Corrosion of Metals (Second Edition), Elsevier, 2016.